Linear-response description of superexchange-driven orbital ordering in K_2CuF_4

Julian Musshoff,[1,2] Guoren Zhang,[3] Erik Koch,[1] and Eva Pavarini[1]

[1]*Institute for Advanced Simulation, Forschungszentrum Jülich, 52425 Jülich, Germany*
[2]*Department of Physics, RWTH Aachen University, 52074 Aachen, Germany*
[3]*Key Laboratory of Materials Physics, Institute of Solid State Physics, Chinese Academy of Sciences,
Hefei 230031, People's Republic of China*

We study the nature of orbital and magnetic order in the layered perovskite K_2CuF_4, and compare to the case of the infinite-layer system $KCuF_3$. To this end, we augment the local-density approximation + dynamical mean-field theory technique with linear-response functions. We explain orbital and magnetic order, and their evolution with increasing pressure. We show that both the tetragonal (ε_T) and the Jahn-Teller (ε_{JT}) crystal-field splitting play a key role. We find that surprisingly, unlike in $KCuF_3$, ε_T is comparable to, or even larger than, ε_{JT}; in addition, ε_T is mostly determined by the layered structure itself and by the compression of the K cage, rather than by the deformations of the CuF_6 octahedra. Next, we study the nature of orbital order. We calculate the superexchange transition temperature, finding $T_{KK} \sim 300$ K, a value close to the one for $KCuF_3$. Thus, in K_2CuF_4 as in $KCuF_3$, T_{KK} is too small to explain the existence of orbital order up to the melting temperature. We show, however, that in the case of the layered perovskite, an additional superexchange mechanism is at work. It is an orbital Zeeman term, $\hat{h}_{KK}$, and it is active also above T_{KK}. We show that due to $\hat{h}_{KK}$, phases with different types of ordering can coexist at temperatures below T_{KK}. Similar effects are likely to play a role in other layered correlated systems.

I. INTRODUCTION

Orbitally ordered systems have for decades been at the center of an intense debate. The key question concerns the microscopic origin of orbital order and of the associated structural distortions. Historically, two competing mechanisms have been proposed, the purely electronic Kugel-Khomskii [1,2] superexchange interaction and the electron-phonon driven Jahn-Teller coupling [3].

For the classical textbook examples of orbitally ordered materials, the infinite-layer systems $KCuF_3$ and $LaMnO_3$, we have shown [4,5] that Kugel-Khomskii superexchange alone yields transition temperatures T_{KK} too small to justify the existence of orbital order up to the melting temperature. A static crystal field, arising from lattice distortions, is necessary to explain the experimental data. In its presence, orbital fluctuations are strongly suppressed [4–6], thus favoring an orbitally ordered phase. Indeed, in this situation, the order parameter, the orbital polarization $p(T)$, can remain large at very high temperatures, even if the crystal-field splitting is very small compared to the bandwidth [4,5]. The natural conclusion seems to be that for $T \gg T_{KK}$, the experimental structural distortions, and thus the associated static crystal field, can be explained via the electron-phonon Jahn-Teller mechanism. Very recently, we have, however, shown that in the case of $KCuF_3$, not even this is correct. Only accounting for the Born-Mayer repulsion, one can correctly describe the experimentally observed increase of the distortions with temperature or (chemical) pressure [7].

While this settles the case for $KCuF_3$, one should not forget that $KCuF_3$ is an infinite-layered compound. Many orbitally ordered systems have instead a layered structure
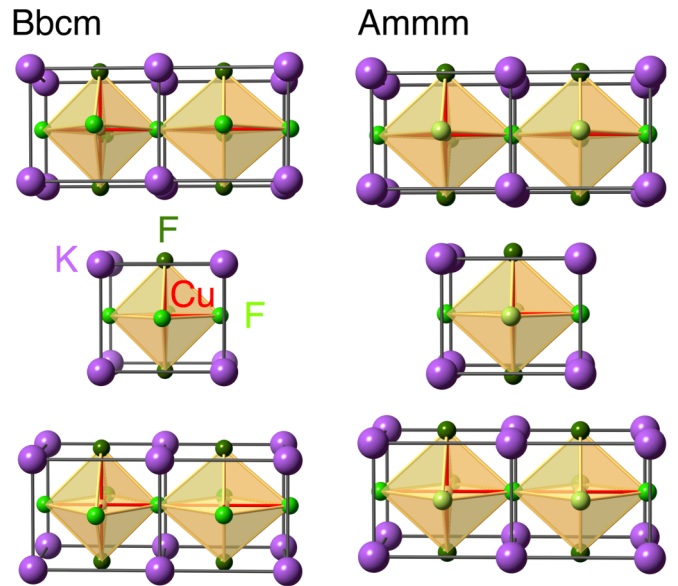

FIG. 1. Layered perovskite crystal structure of K_2CuF_4 [8–19]. Left: *Bbcm* ambient-pressure crystal, showing the antiferro "Jahn-Teller"-like alternation of long and short CuF bonds of the CuF_6 octahedra in the *ab* plane. Right: *Ammm* high-pressure structure with ferro arrangement of long and short CuF bonds and compression of the cubic K cage. For the *Bbcm* structure the conventional orthorhombic body-centered unit cell is rotated by 45° with respect to the *Ammm* case, and it contains four instead of two formula units. In the *Bbcm* case, two consecutive layers are shifted by $(\mathbf{a} + \mathbf{b} + \mathbf{c})/2$, while in the *Ammm* case by $(\mathbf{b} + \mathbf{c})/2$.

(see, e.g., Fig. 1 for K$_2$CuF$_4$). Do the same conclusions apply in those cases? Layered materials are qualitatively different because, as shown in this paper, by symmetry, the structure yields by itself not only a static tetragonal crystal field but also a superexchange-induced orbital field. The latter could suppress orbital fluctuations and favor orbital order at very high temperatures, even without any actual phase transition. In this work, we address this point, clarifying the nature and the importance of these effects.

The system for which these effects can be best studied is the charge transfer insulator K$_2$CuF$_4$. It belongs to the K$_{n+1}$Cu$_n$F$_{3n+1}$ series [8–23], which includes KCuF$_3$ as the infinite-layer limit. This allows a direct comparison of all effects and their strength. The single-layered K$_2$CuF$_4$ is a rare example of a transparent orbitally ordered Heisenberg ferromagnet [18,20] and has a Curie temperature $T_C \sim 6$ K. It has been experimentally shown that in this system the magnetic order changes from ferro- to antiferromagnetic by increasing pressure, following a change in crystal structure (*Bbcm* to *Ammm*) and orbital order [21]. The *Bbcm* and *Ammm* crystal structures are compared in Fig. 1. In this paper, we study superexchange effects and their interplay with actual distortions in the two phases. We determine the actual strength of the Kugel-Khomskii coupling for orbital ordering. In addition, we clarify the role played by the superexchange orbital Zeeman field. Finally, we emphasize the differences in behavior between K$_2$CuF$_4$ and the infinite-layer compound KCuF$_3$.

The paper is organized as follows. In Sec. II we describe the model used and the method of solution adopted. We study the problem via the local-density approximation + dynamical mean-field theory (LDA+DMFT) approach. In order to calculate the strength of the superexchange couplings and the associated transition temperature T_{KK} we use two approaches. The first was developed in Ref. [4] and has already been used with success in a number of additional cases, e.g., Ref. [5] and Refs. [24–26]. It is based on the calculation of the order parameter, the orbital polarization $p(T)$, as a function of temperature and for decreasing distortions. This allows us to study orbital ordering for specific **q** vectors. The second approach is based on linear-response functions. It allows us to compare competing types of ordering and to better single-out the effects of the different terms of the superexchange interaction. In Sec. III we present the results. We show that T_{KK} itself is close to the value for the infinite-layer system KCuF$_3$. We show furthermore that the orbital Zeeman interaction $\hat{h}_{KK}$ yields a finite orbital polarization even for $T > T_{KK}$. Although this orbital polarization is small for K$_2$CuF$_4$, our results indicate that it could be larger in other systems. Furthermore, we find that due to $\hat{h}_{KK}$, two orbitally ordered phases can coexist for $T < T_{KK}$. In Sec. IV we draw our conclusions. In the appendices we give details on the orbital field and the approach used for linear-response function calculations.

II. MODEL AND METHOD

We use the local-density approximation plus dynamical mean-field theory (LDA+DMFT) approach [27–31]. First we calculate the electronic structure in the local-density approx-
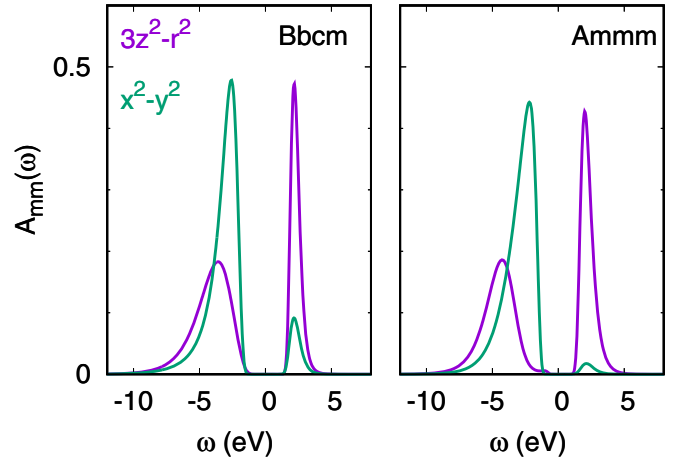

FIG. 2. Orbital-resolved spectral function (in states/Cu/spin/eV) for the ambient-pressure *Bbcm* structure (left) and the *Ammm* high-pressure structure (right) at 290 K for $U = 7$ eV and $J = 0.9$ eV.

imation (LDA) via the full-potential linearized augmented plane-wave method as implemented in the WIEN2k code [32]. Then, via the maximally localized Wannier function method [33,34] and e_g projectors, we construct localized e_g-like Wannier functions centered at the Cu atoms, spanning the e_g bands. Using these Wannier orbitals we build the e_g Hubbard Hamiltonian

$$H = -\sum_{ii'\sigma} \sum_{mm'} t_{m,m'}^{i,i'} c_{im\sigma}^{\dagger} c_{i'm'\sigma}$$
$$+ \frac{1}{2} \sum_{i\sigma\sigma'} \sum_{mm'pp'} U_{mm'pp'} c_{im\sigma}^{\dagger} c_{im'\sigma'}^{\dagger} c_{ip'\sigma'} c_{ip\sigma}, \quad (1)$$

where $c_{im\sigma}$ ($c_{im\sigma}^{\dagger}$) annihilates (creates) an electron at lattice site i with spin $\sigma \in \{\uparrow, \downarrow\}$ and orbital quantum number $m \in \{x^2-y^2, 3z^2-r^2\}$. The one-electron terms $-t_{m,m'}^{i,i'}$ yield hopping integrals ($i \neq i'$) and the crystal-field matrix ($i = i'$). All screened Coulomb parameters $U_{mm'pp'}$ can be expressed in terms of U and J, the direct and exchange screened Coulomb terms; for the latter, we adopt the values established in previous works on similar compounds [4], $U = 7$ eV and $J = 0.9$ eV. As quantum impurity solver we use the generalized hybridization-expansion continuous-time quantum Monte Carlo (CT-HYB QMC) method [35] in the implementation presented in Ref. [24]; this solver, in the Krylov version, can be used for systems of any symmetry. We perform LDA+DMFT calculations for the experimental structure at ambient and high pressure and for a number of idealized structures obtained by progressively removing the distortions. In Fig. 2 we show the orbital-resolved spectral functions for the two experimental structures. For each of them we calculate the temperature dependence of the order parameter, the orbital polarization $p(T)$. The latter is defined as the difference $p(T) = n_1 - n_2$, where n_i are the occupations of the natural orbitals, ordered such that $n_1 > n_2$. Thus $0 \leqslant p(T) \leqslant 1$, where $p(T) = 0$ in the paraorbital phase and $p(T) = 1$ in the fully orbitally ordered state.

In addition, we calculate the local spin and orbital susceptibilities [36]. The latter are given by

$$\chi_{\alpha\alpha}^{\hat{X}\hat{X}}(\tau) = \langle \mathcal{T}\hat{X}_\alpha(\tau)\hat{X}_\alpha(0)\rangle - \langle \hat{X}_\alpha(0)\rangle\langle \hat{X}_\alpha(0)\rangle$$

with $\alpha = x, z$ and $\hat{X} = \hat{S}, \hat{O}$. Here $\hat{S}_\alpha$ are spin and $\hat{O}_\alpha$ orbital pseudospin operators. The spin operators are defined as $\hat{S}_z = \frac{1}{2}\sum_{m\sigma}\lambda_\sigma c_{m\sigma}^\dagger c_{m\sigma}$, with $\lambda_\sigma = \delta_{\sigma,\uparrow} - \delta_{\sigma,\downarrow}$, and $\hat{S}_x = \frac{1}{2}\sum_m \sum_{\sigma\neq\sigma'} c_{m\sigma}^\dagger c_{m\sigma'}$. By analogy, the orbital pseudospin operators are defined respectively as $\hat{O}_z = \frac{1}{2}\sum_{m\sigma}\lambda_m c_{m\sigma}^\dagger c_{m\sigma}$ with $\lambda_m = \delta_{m,x^2-y^2} - \delta_{m,3z^2-r^2}$ and $\hat{O}_x = \frac{1}{2}\sum_\sigma \sum_{m\neq m'} c_{m\sigma}^\dagger c_{m'\sigma}$.

In order to calculate the local susceptibilities we extend our CT-HYB QMC solver to two-particle Green's functions. Depending on the case, we calculate the latter either in the Legendre [37] or in the so-called intermediate representation [38]. Simulations based on the latter are sizably faster. This is because, in the intermediate representation, both the one- and two-particle Green's functions decay very quickly with increasing polynomial order l. In typical cases, $l_{\max}$, the maximum value of l needed in the intermediate representation, can be about half of the corresponding value for the Legendre representation.

With respect to the case of one-particle Green's functions, linear-response functions are computationally more challenging. Using symmetries and massive parallelization we can strongly reduce the actual computational time for a fixed accuracy. Finally, we obtain the lattice susceptibilities in the local-vertex approximation by solving the Bethe-Salpeter equation. More details on the implementation of the calculations of linear-response functions can be found in the appendices. In all cases considered, at sufficiently high temperature—not so high, however, that charge fluctuations become important—we find that the static susceptibility behaves as the static mean-field susceptibility of a generalized superexchange model; i.e., it has the form

$$\chi_{\alpha\alpha}^{\hat{X}\hat{X}}(\mathbf{q};0) \sim \frac{\mu_X^2}{k_B T + \Gamma_{\alpha\alpha}^X(\mathbf{q})/\mu_X^2},$$

where $\alpha = x, y, z$ indicates the direction and μ_X is the effective moment for the orbital ($\hat{X} = \hat{O}$) and spin ($\hat{X} = \hat{S}$) susceptibility. This allows us to extract from the high-temperature susceptibility the function $\Gamma_{\alpha\alpha}^X(\mathbf{q})$, the effective superexchange coupling for a given $\mathbf{q}$ vector, and thus to study its momentum dependence and the possible instabilities of a given system. We have already shown this explicitly in Ref. [39] for the spin susceptibility of the weakly frustrated system VOMoO$_4$. In the specific cases discussed here, the effective local moment takes the value $\mu_X \sim 1/2$ for both the orbital and spin susceptibilities.

III. RESULTS

A. Orbital and spin order

Let us start from the experimental structure and discuss the orbital order emerging from our LDA+DMFT calculations. To this end, we diagonalize the DMFT occupation matrix and calculate the orbital occupations and the associated orbital order. At a given site, we define the lower-energy crystal-field orbital as $|\bar{\theta}\rangle = \cos\frac{\theta}{2}|3z^2 - r^2\rangle + \sin\frac{\theta}{2}|x^2 - y^2\rangle$ and the

higher-energy orbital as $|\theta\rangle = -\sin\frac{\theta}{2}|3z^2 - r^2\rangle + \cos\frac{\theta}{2}|x^2 - y^2\rangle$. In the case of the *Bbcm* structure, the corresponding crystal-field orbitals at a neighboring site in the xy plane can be obtained via the transformation $x \leftrightarrow y$. In the case of the *Ammm* high-pressure structure, the crystal-field orbital is the same at all sites in a given plane. For all structures, we find that at each site, the associated lowest-energy crystal-field state is fully occupied even at very high temperature, i.e., $p(T) \sim 1$. This corresponds to antiferro orbital order in the *Bbcm* structure and ferro orbital order in the *Ammm* structure, in line with experiments.

We now consider in more detail the relative weight of Jahn-Teller and tetragonal crystal-field splitting in determining the occupied states. Table I shows that surprisingly, in the high-pressure phase (*Ammm*) the crystal-field matrix has a dominant tetragonal term, $\varepsilon_T = \varepsilon_{3z^2-r^2} - \varepsilon_{x^2-y^2} = t_{0,0}^{i,i} - t_{\pi,\pi}^{i,i} \sim 434$ meV, while the off-diagonal Jahn-Teller splitting is merely $\varepsilon_{JT} = 2|t_{0,\pi}^{i,i}| \sim 178$ meV, despite an appreciable difference between short and long CuF bonds. For the ambient-pressure structure (*Bbcm*) we find a similar tetragonal splitting, $\varepsilon_T = 460$ meV, but a much larger Jahn-Teller splitting, $\varepsilon_{JT} = 500$ meV. Thus, in the ambient-pressure case, the Jahn-Teller and the tetragonal crystal-field splitting are, surprisingly, comparable, unlike in the infinite-layer system KCuF$_3$. This is reflected in the angle θ defining the natural orbitals, which is halfway between 180°, the value expected from a dominant tetragonal splitting with a hole in the $|3z^2 - r^2\rangle$ state, and 90°, the value expected for a dominant off-diagonal Jahn-Teller splitting. This is shown in Table I. Remarkably, while the Jahn-Teller splitting is entirely or almost entirely due to the deformation of the F$_6$ octahedra, the tetragonal splitting is not. As a matter of fact, it remains sizable even in the case in which the octahedra are artificially made regular (structures B_2 and A_2 in the table), so that all Cu-F bonds are the same, while the K cage remains unchanged. This is because of the joint effect of the layered structure and the compression of the K cage along the c axis.

Based on these results, we then calculate the magnetic exchange couplings. First we use second-order perturbation theory and obtain the expression

$$\Gamma_{SE}^{i,i'} \sim \frac{4|t_{h,h}^{i,i'}|^2(U + \varepsilon_{CF})}{(U + \varepsilon_{CF})^2 - J^2} - \frac{|t_{f,h}^{i,i'}|^2 + |t_{h,f}^{i,i'}|^2}{U + \varepsilon_{CF} - 3J}\frac{2J}{U + \varepsilon_{CF} - J}.$$

Here $t_{\tilde{m},\tilde{m}'}$ with $\tilde{m} = h, f$ are the hopping integrals in the basis $\{f, h\}$ of natural orbitals; $|f\rangle$ is the filled and $|h\rangle$ the half-filled orbital. The parameters appearing in this formula can be obtained from Table I, where the corresponding values of $\Gamma_{SE}^{i,i'}$ are also given. We find that the magnetic coupling in the ab plane is ferromagnetic ($\Gamma_{SE} < 0$) and isotropic at ambient pressure, and switches to antiferromagnetic ($\Gamma_{SE} > 0$) in the short-axis direction under high pressure, when the system changes space group to *Ammm* [15–17]. This is in excellent agreement with experimental results [18].

We point out that this is a very strong test for our modeling of K$_2$CuF$_4$. Indeed, the magnetic couplings are very sensitive to small structural changes. For example, without Jahn-Teller distortion (A_1 and B_1 cases in Table I) the couplings would be in all cases antiferromagnetic, and for the high-pressure

TABLE I. Hopping integrals $t^{i,i'}_{m,m'}$ between site i' and $i \sim i' + l\mathbf{x} + m\mathbf{y} + n\mathbf{z}$, in meV. The axes are defined as $\mathbf{x} = (\mathbf{a} + \mathbf{b})/2$, $\mathbf{y} = (-\mathbf{a} + \mathbf{b})/2$, $\mathbf{z} = \mathbf{c}$ for the *Bbcm* structure and as $\mathbf{x} = \mathbf{a}$, $\mathbf{y} = \mathbf{b}$, $\mathbf{z} = \mathbf{c}$ for the *Ammm* structure. The orbitals m are labeled here as $|\bar{\pi}\rangle = |x^2 - y^2\rangle$ and $|\bar{0}\rangle = |3z^2 - r^2\rangle$. Results for *Bbcm* (*Ammm*) structures with artificially reduced distortions are labeled B_α (A_α). In particular, $\alpha = 1$: no Jahn-Teller distortion of the octahedra; $\alpha = 2$: regular CuF$_6$ octahedra. The magnetic superexchange couplings in the *ab* plane obtained from second-order perturbation theory, $\Gamma^{i,i'}_{SE}$, are also given. The angle θ given in parentheses identifies for each structure the crystal-field state with the lowest energy, the state labeled with $|\bar{\theta}\rangle$ in the main text. Due to the different stacking of the layers along $\hat{z}$ (see Fig. 1 and its caption), the Cu site symmetry is D_{4h} for the B_2 structure and D_{2h} for the A_2 structure.

lmn	$t^{i,i'}_{0,0}$	$t^{i,i'}_{\pi,0}$	$t^{i,i'}_{0,\pi}$	$t^{i,i'}_{\pi,\pi}$	$\Gamma^{i,i'}_{SE}$	$t^{i,i'}_{0,0}$	$t^{i,i'}_{\pi,0}$	$t^{i,i'}_{0,\pi}$	$t^{i,i'}_{\pi,\pi}$	$\Gamma^{i,i'}_{SE}$
	Bbcm ($\theta = 132.6°$)					*Ammm* ($\theta = 157.6°$)				
000	−306	−250	−250	−766		−279	−89	−89	−713	
100	−107	131	173	−217	−3.6	−149	206	206	−292	24
010	−107	−173	−131	−217	−3.6	−98	−157	−157	−272	−0.4
	B_1 ($\theta = 180°$)					A_1 ($\theta = 179.3°$)				
000	−274	0	0	−691		−327	−3	−3	−802	
100	−115	159	159	−224	4.3	−121	183	183	−280	4.4
010	−115	−159	−159	−224	4.3	−131	−184	−184	−280	5.2
	B_2 ($\theta = 180°$)					A_2 ($\theta = 175.6°$)				
000	−252	0	0	−581		−317	−16	−16	−729	
100	−93	144	144	−226	2.3	−114	177	177	−281	5.0
010	−93	−144	−144	−226	2.3	−127	−179	−179	−281	3.5

structure the couplings would be even almost isotropic. This is mostly due to the changes in the actual occupied orbital. The experimental magnetic structure can only be explained when both tetragonal and Jahn-Teller distortions are taken into account, as Table I shows.

Let us now go a step further and calculate the magnetic superexchange couplings via linear-response theory. First we calculate the spin susceptibility in the high-temperature regime (not so high, however, that charge fluctuations play a role), where it is described by

$$\chi^{\hat{S}\hat{S}}_{zz}(\mathbf{q};0) \sim \frac{\mu_S^2}{k_B T + \Gamma^s_{zz}(\mathbf{q})/\mu_S^2}.$$

In this regime we find that the effective magnetic moment, which we obtain independently from the correlation function, is $\mu_S \sim 1/2$. Next we extract from the formula above the effective magnetic couplings $\Gamma^s_{zz}(\mathbf{q}) = \Gamma^s_{xx}(\mathbf{q}) = \Gamma^s_{yy}(\mathbf{q})$ and their **q** dependence. The results are shown in Fig. 3. The figure shows that for the *Bbcm* structure the dominant magnetic vector is $\mathbf{q} = \mathbf{0}$ (ferromagnetic); the associated coupling is $\Gamma^s_{zz}(\mathbf{0}) \sim 4\Gamma^{i,i+\mathbf{x}}_{SE}$. Instead, for the *Ammm* structure, the exchange coupling is semi-one-dimensional, and the magnetic vector is $\mathbf{q} = X$ (antiferromagnetic), while $\Gamma^s_{zz}(\mathbf{0}) \sim 2\Gamma^{i,i+\mathbf{x}}_{SE}$. Linear-response calculations confirm that switching to structure B_1 or A_1 (no Jahn-Teller distortion of the octahedra) reverses the sign of the magnetic couplings, which become in both cases antiferromagnetic and almost isotropic. The values we obtain from linear-response theory are close to those from second-order perturbation theory given in Table I; this indicates that longer-range terms and higher-perturbation orders, in all the cases considered, only weakly change the effective magnetic couplings. In Fig. 3 we show that this effect is even stronger (i.e., it yields larger antiferromagnetic

couplings) if we, in addition, set the crystal field to zero (B_1 and A_1 panels). Finally, if the octahedra are artificially made completely regular (B_2 and A_2 structures), while keeping the cation cubic cage unmodified, the remaining changes are small. This is again shown in Fig. 3.
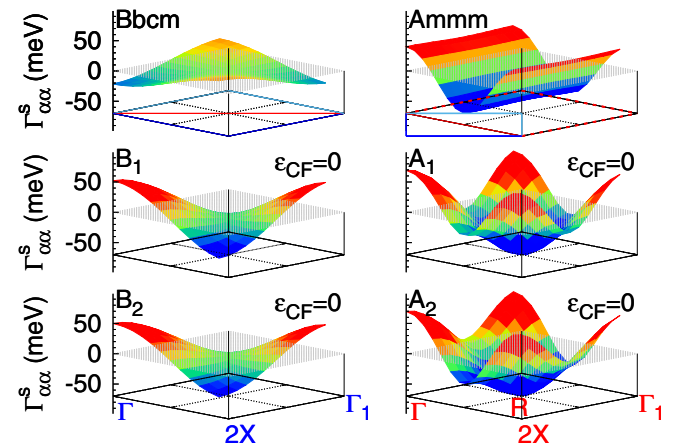

FIG. 3. Effective magnetic exchange couplings $\Gamma^S_{\alpha,\alpha}(\mathbf{q})$, with $\alpha = x, y, z$, for the *Bbcm* structure (left) and the *Ammm* high-pressure structure (right) for $U = 7$ eV and $J = 0.9$ eV, as obtained via linear-response theory. For the *Bbcm* structure, the **x** and **y** axes are rotated by $\pi/4$ with respect to the *Ammm* structure. This is shown in the two upper panels, bottom surfaces. The special points are $\Gamma = (0, 0, 0) = \mathbf{0}$, $\Gamma_1 = (2\pi, 2\pi, 2\pi)$, $2X = (2\pi, 0, 0)$, $R = (\pi, \pi, \pi)$. On the opposite side of $2X$ is the point $2Y_1 = (0, 2\pi, 2\pi)$. All lattice constants are set equal to 1 for simplicity. The expected magnetic-ordering vector is the value of **q** for which the magnetic exchange coupling $\Gamma^s_{\alpha\alpha}(\mathbf{q})$ is most negative. In the case of the idealized structures B_1, B_2 and A_1, A_2 (see text) the crystal field is set to zero.
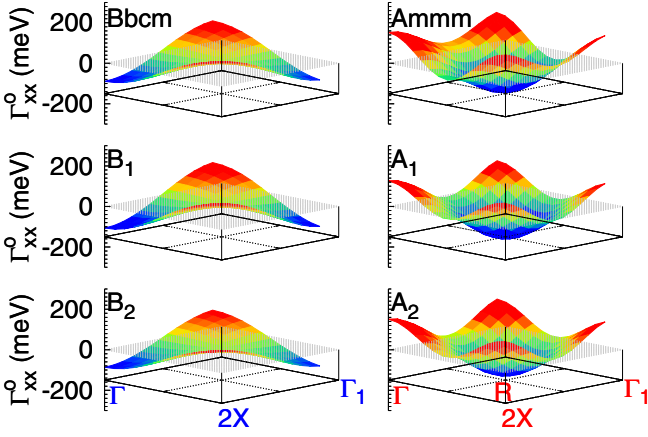
FIG. 4. Effective orbital exchange couplings Γ_{xx}^o for the *Bbcm* structure (left) and the *Ammm* high-pressure structure (right) for $U = 7$ eV and $J = 0.9$ eV. The special points are $\Gamma = (0, 0, 0)$, $\Gamma_1 = (2\pi, 2\pi, 2\pi)$, $2X = (2\pi, 0, 0)$, $R = (\pi, \pi, \pi)$. On the opposite side of $2X$ is the point $2Y_1 = (0, 2\pi, 2\pi)$. The difference between the **x** and **y** directions of the *Ammm* and *Bbcm* structures is illustrated in Fig. 3, top panels. The crystal field is set to zero in all cases.

B. Superexchange critical temperature T_{KK} and orbital Zeeman interaction $\hat{h}_{KK}$

Based on the success in describing and explaining magnetic and orbital order, in this section we study the orbital superexchange couplings and the possible instabilities arising from them. The results of linear-response theory calculations are shown in Figs. 4 and 5. They show that for the experimental ambient-pressure structure (*Bbcm*), the favored instability is at the Γ point. Such an ordering vector yields a type of orbital order that has the same space group as the experimental crystal. It corresponds approximately to $|\theta\rangle =$
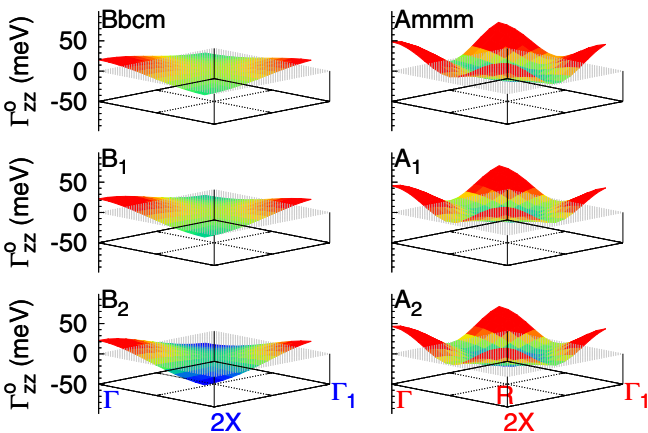

FIG. 5. Effective orbital exchange couplings Γ_{zz}^o for the *Bbcm* structure (left) and the *Ammm* high-pressure structure (right) for $U = 7$ eV and $J = 0.9$ eV. The special points are $\Gamma = (0, 0, 0)$, $\Gamma_1 = (2\pi, 2\pi, 2\pi)$, $2X = (2\pi, 0, 0)$, $R = (\pi, \pi, \pi)$. On the opposite side of $2X$ is the point $2Y_1 = (0, 2\pi, 2\pi)$. The difference between the **x** and **y** directions of the *Ammm* and *Bbcm* structures is illustrated in Fig. 3, top panels. The crystal field is set to zero in all cases.

$|90°\rangle$, i.e., to hole orbitals close to $|s^2 - z^2\rangle$, where s is the short CuF bond; short and long bonds alternate along $\hat{x}$ and $\hat{y}$. This has two reasons. First, for all **q** vectors, $|\Gamma_{zz}^o(\mathbf{q})|$ is significantly smaller than $|\Gamma_{xx}^o(\mathbf{0})|$, as may be seen comparing the vertical scales of Figs. 4 and 5. Second, Γ is the **q** vector for which the (dominant) exchange coupling $\Gamma_{xx}^o(\mathbf{q})$ is most negative. Figure 5 shows in addition that in the hypothetical cases in which we could set $\Gamma_{xx}^o(\mathbf{0}) = 0$, by itself, the $\Gamma_{zz}^o(\mathbf{q})$ coupling would favor the $\mathbf{q} = 2X$ ordering vector; this yields an alternation of $|3z^2 - r^2\rangle$ and $|x^2 - y^2\rangle$ as hole orbitals, a quite exotic orbitally ordered structure. At the Γ point, instead, $\Gamma_{zz}^o(\mathbf{q}) > 0$ (energy loss). This can lead to frustration.

The situation is more extreme for the *Ammm* structure. Here both couplings $\Gamma_{zz}^o(\mathbf{q})$ and $\Gamma_{xx}^o(\mathbf{q})$ yield an energy loss at the Γ point. Indeed, $\Gamma_{xx}^o(\mathbf{q})$ favors instead antiferro orbital order with the same arrangement as in the ambient-pressure structure case, despite the ferro orbital crystal field. This can be seen from the fact that the most negative value of $\Gamma_{xx}^o(\mathbf{q})$ is at the R point of the *Ammm* Brillouin zone in Fig. 4. The R point is also the ordering vector favored by $\Gamma_{zz}^o(\mathbf{q})$, as can be seen in Fig. 5. The ordering that would emerge from $\Gamma_{zz}^o(R)$ alone differs, however, from the one favored by $\Gamma_{xx}^o(R)$. Indeed $\Gamma_{zz}^o(R)$ alone would yield antiferro orbital order with the alternation of $|3z^2 - r^2\rangle$ and $|x^2 - y^2\rangle$ hole orbitals. It has to be noticed that the effective antiferro orbital couplings for the *Ammm* structure are all small compared to the case of the *Bbcm* structure.

Finally, we point out a remarkable difference between the magnetic superexchange couplings, shown in Fig. 3 and discussed in Table I, and the orbital superexchange couplings shown in Figs. 4 and 5. While the first—in particular in the ferromagnetic case—are quite sensitive to even small structural distortions, the latter are rather robust and depend much less on slight changes, as one can see by comparing the results for the real *Bbcm* structure with those for the idealized B_1 and B_2 unit cells, and the results for the real *Ammm* structure with those for the idealized A_1 and A_2 unit cells.

These results rule out the intersite superexchange Kugel-Khomskii coupling as the possible dominant mechanism determining orbital order. This is in line with the conclusion we have previously reached for infinite-layer perovskites [4,5,7]. For the high-pressure structure, we find that superexchange would even predict a *different* orbital structure than experimentally observed.

As we pointed out in the introduction, layered materials are however different from their infinite-layer counterparts, because layered tetragonal symmetry alone allows for a superexchange term of the form

$$\hat{h}_{KK} = \sum_i \hat{B}_z^{KK} \hat{O}_z^i.$$

For a e_g^3 tight-binding Hubbard model of a tetragonal layered perovskite the operator $\hat{B}_z^{KK}$ is given by (see Appendix A)

$$\hat{B}_z^{KK} = -N_i \frac{\Gamma}{2} \sum_{i' \neq i} \left[\hat{\mathbf{S}}^i \cdot \hat{\mathbf{S}}^{i'} - \frac{n_i n_{i'}}{4} \right] \frac{n_{i'}}{2},$$

where N_i is the number of neighbors coupled via superexchange, $\Gamma = 4t^2/U$, and the n_i operator yields the occupation of site i. Thus the term $\hat{h}_{KK}$ acts as an effective orbital
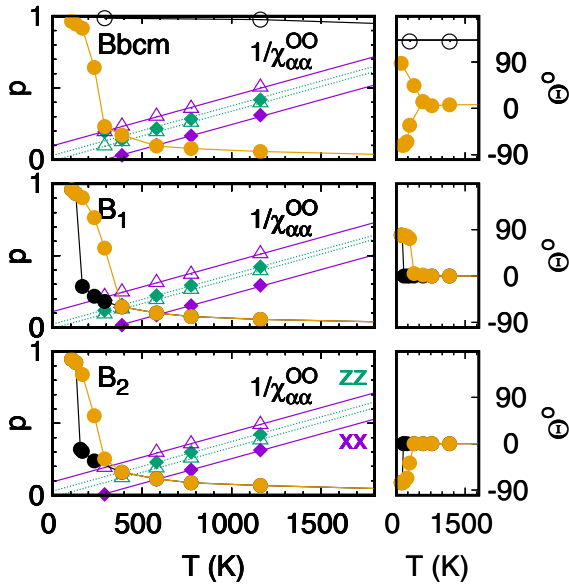
FIG. 6. *Bbcm* (ambient-pressure) structure. Left top panel, empty circles: orbital polarization $p(T)$ for the experimental structure. Left panels, filled circles: orbital polarization $p(T)$ in the absence of crystal-field splitting. For B_1 and B_2, two different solutions coexist (lighter/darker circles) between 150 K and 300 K. Left panels, straight lines: linear fit of the inverse orbital susceptibility $1/\chi_{\alpha\alpha}^{OO}(\mathbf{q}; 0)$ at specific $\mathbf{q}$ points. Diamonds: $\mathbf{q} = \mathbf{0}$. Triangles: $\mathbf{q} = 2X$. Solid lines: $\alpha = x$. Dashed lines: $\alpha = z$. Right panels, filled circles: angle θ defining the hole state in the absence of crystal-field splitting. Two solutions with angles $\pm\theta$ are equivalent. The black line in the top right panel is the value of θ for the LDA ground crystal-field state.
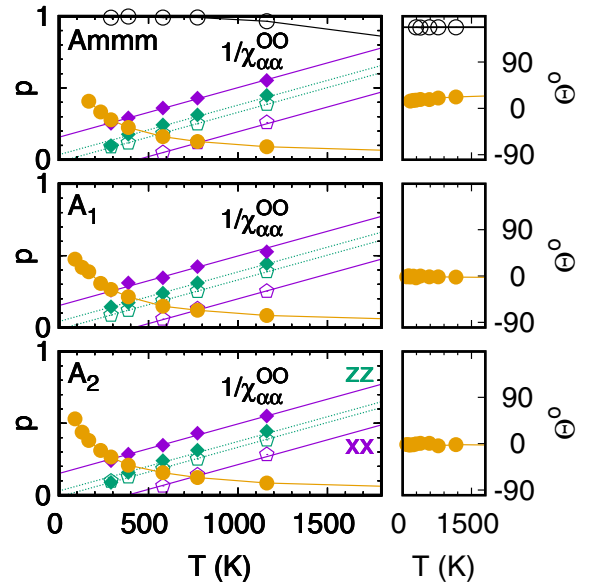
FIG. 7. *Ammm* (high-pressure) structure. Left top panel, empty circles: orbital polarization $p(T)$ for the experimental structure. Left panels, filled circles: orbital polarization $p(T)$ in the absence of crystal-field splitting. Left panels, straight lines: linear fit of the inverse orbital susceptibility $1/\chi_{\alpha\alpha}^{OO}(\mathbf{q}; 0)$ at specific $\mathbf{q}$ points. Diamonds: $\mathbf{q} = \mathbf{0}$. Pentagons: $\mathbf{q} = R$. Solid lines: $\alpha = x$. Dashed lines: $\alpha = z$. Right panels, filled circles: angle θ defining the hole state in the absence of crystal-field splitting. The black line in the top right panel is the value of θ for the LDA ground crystal-field state.

Zeeman interaction when ferromagnetic spin correlations are negligible. For K_2CuF_4 the Curie temperature is very small, and therefore ferromagnetic fluctuations are negligible in the temperature range of interest here. In the infinite-layer limit $\hat{h}_{KK}$ is zero by symmetry.

In order to single out the effect of $\hat{h}_{KK}$, we calculate the order parameter and the associated orbital polarization as a function of the temperature. The results are shown in Fig. 6 for the ambient-pressure structure and in Fig. 7 for the high-pressure structure. In the ambient-pressure case, we find that $\hat{h}_{KK}$ generates an orbital polarization well above $T_{KK} \sim 300$ K. The associated occupations correspond to a $|x^2 - y^2\rangle$ hole state. Since $\hat{h}_{KK}$ acts as a Zeeman interaction, the orbital polarization is not associated with a phase transition. Furthermore, in this specific case, the orbital Zeeman term $\hat{h}_{KK}$ does not favor the superexchange-driven orbital order *transition* itself. In fact, it favors $|\theta = 0°\rangle$ as the hole state, while the intersite superexchange couplings favor $|\theta = 90°\rangle$, as we have seen above. Hence $\hat{h}_{KK}$, in general, effectively reduces the actual transition temperature T_{KK}, similarly to what we found a static tetragonal crystal field does for manganites [26]. When the temperature is lowered through T_{KK}, the actual superexchange phase transition takes place and the hole moves to the $|\theta = 90°\rangle$ state. Two phases, one in which the orbital polarization is small and the hole state is $|\theta\rangle = |0°\rangle$, and one in which the orbital polarization is large and the hole

state is $|\theta\rangle = |90°\rangle$, can also coexist, however. This is shown in the lower panels of Fig. 6.

Even more remarkable are the results for the high-pressure phase. Here the superexchange phase transition is not allowed for $\mathbf{q} = \mathbf{0}$, i.e., for the experimental structure, since the superexchange interaction favors critical vectors other than $\mathbf{q} = \mathbf{0}$, as we have discussed previously. Hence, the polarization induced by $\hat{h}_{KK}$ continues to grow on lowering the temperature, and reaches ~ 0.5 at about 100 K. This yields orbital order at low temperature, despite the fact that the superexchange intersite coupling yields an energy loss, and that there is no phase transition at all. The hole state is again $|x^2 - y^2\rangle$. It is interesting to compare now with the hole state for the experimental structure, including thus the actual crystal field. The figure shows that $|\theta\rangle \sim |180°\rangle$. This is because the tetragonal static crystal field ε_T is very large and, in addition, the $|x^2 - y^2\rangle$ state is lower in energy than the $|3z^2 - r^2\rangle$ (see Table I). Thus $\hat{h}_{KK}$ actually competes with ε_T in the case of K_2CuF_4. Its global effects are however small, as one can see from the fact that in Figs. 6 and 7 the occupied state obtained in DMFT is very close to the one obtained in LDA.

Thus, in K_2CuF_4, the term $\hat{h}_{KK}$ induces an orbital polarization at temperature $T \gg T_{KK}$. However, the effects of $\hat{h}_{KK}$ compete with those of the static crystal field; even in its absence ($\varepsilon_T = 0$), the total orbital polarization is small in the high-temperature regime. Our results therefore confirm for the layered perovskite K_2CuF_4 the conclusions we already have reached for the infinite-layer system $KCuF_3$. Superexchange (in all its contributions) is not sufficient alone to

explain the presence of orbital order at very high temperatures. Nevertheless, our work also shows where layered systems are qualitatively different from infinite-layered compounds: There are superexchange orbital Zeeman terms. In covalent materials in which the hopping integrals are larger and the Coulomb repulsion is smaller than in K_2CuF_4, these terms should play an important role.

IV. CONCLUSION

We have calculated magnetic and orbital order in single-layered K_2CuF_4, at ambient and high pressures. When we use experimental structures, we find excellent agreement with experiments. In particular, we can explain the change in orbital order with pressure, and the associated change in magnetic structure. Based on this success, we studied the role of superexchange in determining orbital order. We have shown that T_{KK}, the superexchange transition temperature, is $\sim$300 K for the ambient-pressure structure. This value is close to the one we previously obtained for the infinite-layer system $KCuF_3$. By using linear-response calculations, we have shown that for the $Ammm$ phase, the superexchange-only orbital-ordering vector is not compatible with the experimental structure. This is remarkable by itself, since at ambient pressure, in most orbitally ordered systems the opposite is true [40]; a situation of this kind is only realized at high pressure. Furthermore, we have shown that there is an additional superexchange-based mechanism that can lead to orbital order. This is due to the superexchange orbital Zeeman field, which is zero in the infinite-layer limit. Such a mechanism results in a finite orbital polarization above the superexchange transition temperature T_{KK} and can lead to coexisting phases below T_{KK}. This orbital Zeeman field, together with the static crystal field, can give rise to orbital ordering also at temperature $T > T_{KK}$. For K_2CuF_4 we find, however, that the orbital Zeeman field and the associated polarization is small at high temperature. Furthermore the hole orbital corresponds to $|x^2 - y^2\rangle$. Thus the orbital field cannot alone drive orbital ordering in K_2CuF_4 at high temperature. As in the case of the infinite-layered material $KCuF_3$, experimental results can only be explained accounting for a static crystal field, determined by the actual crystal-field distortions. Still, our results indicate the orbital Zeeman field could play a larger role in more covalent layered compounds, where the hopping integrals and the superexchange couplings are larger.

ACKNOWLEDGMENTS

APPENDIX A: ORIGIN OF SUPEREXCHANGE-DRIVEN ORBITAL ZEEMAN FIELD: A TOY MODEL

Here we discuss the origin of the superexchange-driven orbital Zeeman field. We adopt as an example the case of an ideal ABC_3 perovskite with the e_g^1 configuration; we set $J = 0$

for keeping the discussion simple [41]. In the tight-binding approximation, only hopping integrals between neighboring B sites in the cubic perovskite structure play a role. The hopping integral matrices along the (001) direction have, in first approximation, the simple form

$$t_{m,m'}^{i,i\pm\hat{z}} \sim t \begin{pmatrix} 1 & 0 \\ 0 & 0 \end{pmatrix},$$

where we ordered the orbital as $|3z^2 - r^2\rangle$ and $|x^2 - y^2\rangle$. Let us consider at first only pairs of sites along the $\hat{z}$ axis, chosen as the quantization axis, and calculate the superexchange Hamiltonian. In second-order perturbation theory in $\hat{H}_T$, for the e_g^1 configuration we obtain the following superexchange Hamiltonian [1,2]

$$\hat{H}_{KK}^{\hat{z}} \sim \frac{\Gamma}{2} \sum_{ii'} \left[\hat{\mathbf{S}}^i \cdot \hat{\mathbf{S}}^{i'} - \frac{n_i n_{i'}}{4}\right]\left[\hat{O}_z^i - \frac{n_i}{2}\right]\left[\hat{O}_z^{i'} - \frac{n_{i'}}{2}\right]$$
$$+ \frac{\Gamma}{4} \sum_{ii'} \left[\hat{O}_z^i \hat{O}_z^{i'} - \frac{n_i n_{i'}}{4}\right],$$

where $\Gamma = 4t^2/U > 0$. For the e_g^3 configuration an analogous expression can be found, with $\hat{O}_z \to -\hat{O}_z$. The superexchange Hamiltonian above contains the term

$$\hat{h}_{KK}^{\hat{z}} = -\frac{\Gamma}{2} \sum_i \left[\hat{\mathbf{S}}^i \cdot \hat{\mathbf{S}}^{i'} - \frac{n_i n_{i'}}{4}\right]\left[\frac{n_{i'}}{2}\hat{O}_z^i + \hat{O}_z^{i'}\frac{n_i}{2}\right],$$

which can become very weak in the presence of strong ferromagnetic correlations. The superexchange Hamiltonian has the same form if we chose as the quantization axis $\hat{x}$ or $\hat{y}$ instead of $\hat{z}$; to sum up all terms we have merely to rotate back the quantization axis to $\hat{z}$. Hence, we have to make the replacements

$$\hat{O}_z^i \underset{\hat{z}\to\hat{x}}{\longrightarrow} -\frac{1}{2}\hat{O}_z^i - \frac{\sqrt{3}}{2}\hat{O}_x^i,$$

$$\hat{O}_z^i \underset{\hat{z}\to\hat{y}}{\longrightarrow} -\frac{1}{2}\hat{O}_z^i + \frac{\sqrt{3}}{2}\hat{O}_x^i.$$

For an infinite-layer system, after all contributions are summed up, only terms quadratic in the spin and pseudospin operators remain. For a layered structure, however, linear terms do not fully cancel out.

APPENDIX B: CALCULATION OF THE SUSCEPTIBILITY TENSOR

Here we give details on the calculation of the susceptibilities as implemented in our hybridization-expansion continuous-time quantum Monte Carlo (CT-HYB QMC) solver for dynamical mean-field theory (DMFT).

First we calculate the local susceptibility tensor $\chi_{\boldsymbol{\alpha}}(\boldsymbol{\tau})$ for the DMFT quantum-impurity problem. It can be written as the two-particle Green's function tensor, $\mathcal{C}_{\boldsymbol{\alpha}}(\boldsymbol{\tau})$, minus its mean-field component. More specifically

$$\chi_{\boldsymbol{\alpha}}(\boldsymbol{\tau}) = \mathcal{C}_{\boldsymbol{\alpha}}(\boldsymbol{\tau}) - G_{\alpha_1 \bar{\alpha}_2}(\tau_1, \bar{\tau}_2)G_{\alpha_3 \bar{\alpha}_4}(\tau_3, \bar{\tau}_4),$$

with

$$\mathcal{C}_{\boldsymbol{\alpha}}(\boldsymbol{\tau}) = \left\langle \mathcal{T} c_{\alpha_1}(\tau_1) c_{\bar\alpha_2}^\dagger(\bar\tau_2) c_{\alpha_3}(\tau_3) c_{\bar\alpha_4}^\dagger(\bar\tau_4) \right\rangle,$$

$$G_{\alpha_1\bar\alpha_2}(\tau_1, \bar\tau_2) = -\left\langle \mathcal{T} c_{\alpha_1}(\tau_1) c_{\bar\alpha_2}^\dagger(\bar\tau_2) \right\rangle.$$

Here $\boldsymbol{\tau} = (\tau_1, \bar\tau_2, \tau_3, \bar\tau_4)$ and $\mathcal{T}$ is the time-ordering operator. In addition, $\boldsymbol{\alpha} = (\alpha_1, \bar\alpha_2, \alpha_3, \bar\alpha_4)$, where $\alpha_j = m_j \sigma_j i_j$ are collective orbital (m_j), spin (σ_j), and site (i_j) indices; in the expression above, the labels with (without) the bar on top identify imaginary times and flavors for creation (destruction) operators. The generalized local susceptibility tensor is calculated via CT-HYB QMC. To this end, we have extended the implementation described in Ref. [24] to two-particle Green's functions. In CT-HYB QMC the partition function and the one- or two-particle Green's functions are expressed as series expansions in even powers (or orders) of the hybridization. The core of the calculation is the evaluation of the trace over local (quantum impurity) variables. Depending on the specific form of the Hamiltonian, for the calculation of the local trace we use either the (very fast) segment or the (slower but general) Krylov method. Instead of calculating directly $\chi_{\boldsymbol{\alpha}}(\boldsymbol{\tau})$, we express it in a basis of orthogonal functions [37,38] and evaluate those via the CT-HYB QMC approach. The expansion coefficients take the form

$$\chi_{\boldsymbol{\alpha}}^{l,l'}(\omega_m) = \int_0^\beta d\tau_{23} \int_0^\beta d\tau_{12} \int_0^\beta d\tau_{34}\, e^{-i\omega_m \tau_{23}}$$
$$\times\, f_l^m(\tau_{12}) \chi_{\boldsymbol{\alpha}}(\tau_{14}, \tau_{24}, \tau_{34}, 0) f_{l'}^m(\tau_{34}), \quad \text{(B1)}$$

where ω_m is a bosonic Matsubara frequency, while $\tau_{ij} = \tau_i - \tau_j$, with $\tau_{14} = \tau_{12} + \tau_{23} + \tau_{34}$, and $\tau_{24} = \tau_{23} + \tau_{34}$; in order to write the tensor in the form given above, we used the invariance of the trace under rotation of the operators as well as the periodicity (antiperiodicity) of the susceptibility in the bosonic (fermionic) imaginary-time variables. In this work we used two families of functions $f_l^m(\tau)$. The first [37] is defined as

$$f_l^m(\tau) = e^{-i\phi_m(\tau)} \begin{cases} \sqrt{2l+1}\, p_l(x(\tau)), & \tau > 0, \\ -(-1)^m \sqrt{2l+1}\, p_l(x(\tau+\beta)), & \tau < 0, \end{cases}$$

where $p_l(x(\tau))$ is an orthogonal Legendre polynomial of degree l, with $x(\tau) = 2\tau/\beta - 1$. The phase defining the gauge is $\phi_m(\tau) = \omega_m \tau/2$ and does not depend on l; the factor $(-1)^m$ in the second row ensures antiperiodicity for all values of m. The second family of $f_l^m(\tau)$ is obtained replacing $\sqrt{2l+1}\, p_l(x(\tau))$ in the expression above with $\sqrt{2}\, u_l(x(\tau))$; here $u_l(x(\tau))$ is calculated via the singular-value decomposition of $K(x(\tau);\omega) = \frac{e^{-\tau\omega}}{1+e^{-\beta\omega}}$, the kernel for the analytic continuation of the Green's function [38]. The functions $u_l(x(\tau))$ have, by construction, the same symmetry properties in τ as the Legendre polynomials; namely they are symmetric (antisymmetric) about $\beta/2$ for even (odd) l. The expansions described here give a very compact representation of the one- and two-particle Green's function; the representation is even more compact for the numerical functions $u_l(x(\tau))$. This is shown in Fig. 8. The $u_l(x(\tau))$ are calculated once before the QMC simulation starts, in order to reduce the simulation time.

The observables are obtained via Monte Carlo average over the visited configurations c. In the segment approach, the latter are parametrized via time lines (imaginary-time
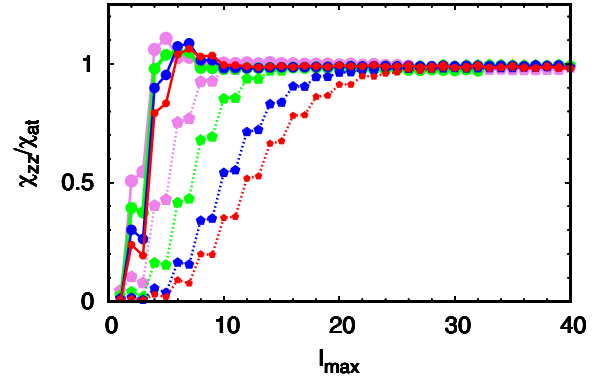

FIG. 8. K_2CuF_4, ambient-pressure structure, B_2-structure parameter set. Convergence of the static local magnetic susceptibility χ_{zz}, normalized to the atomic value, χ_{at}. Here l_{max} (horizontal axis) is the maximum order of the polynomials included in the sum in Eq. (B2). Dashed lines: Legendre polynomials $p_l(x)$. Full lines: $u_l(x)$ polynomials, calculated with a cutoff parameter $\Lambda_{max} \sim \beta U$. Symbols of decreasing size show results for decreasing temperatures, ranging from $\sim$2300 to $\sim$380 K. The figure shows that u_l polynomials converge much faster than Legendre polynomials; the difference in convergence speed increases on lowering the temperature. This can considerably speed-up calculations.

intervals $[0, \beta)$), occupied by a number of creators and annihilators, which in turn define segments on the time lines. The basic Monte Carlo updates are addition and removal of segments, antisegments, or complete lines. In the Krylov approach, we use the insertion and removal of pairs of creation and annihilation operators as basic Monte Carlo updates. In addition, we shift operators in time, introduce global moves (exchange the configurations of blocks) and insertion or deletion of two pairs of creation and annihilation operators. For a given configuration we can evaluate the elements of the susceptibility tensor as follows:

$$\left\langle \chi_{\boldsymbol{\alpha}}^{l,l'}(\omega_m) \right\rangle_c = \left\langle \mathcal{C}_{\boldsymbol{\alpha}}^{l,l'}(\omega_m) \right\rangle_c - \beta \delta_{m,0} \left\langle G_{\alpha_1\bar\alpha_2}^l \right\rangle_c \left\langle G_{\alpha_3\bar\alpha_4}^{l'} \right\rangle_c,$$

where

$$\left\langle \mathcal{C}_{\boldsymbol{\alpha}}^{l,l'}(\omega_m) \right\rangle_c = \frac{1}{\beta} \sum_{bb'dd'}^{N_b} \sum_i^{n_b} \sum_j^{n_d} \sum_{i'}^{n_{b'}} \sum_{j'}^{n_{d'}} W_{dj,bi,d'j',b'i'}^{ll'm\boldsymbol{\alpha}},$$

$$W_{dj,bi,d'j',b'i'}^{ll'm\boldsymbol{\alpha}} = f_l^m(\tau_{dj} - \bar\tau_{bi}) f_{l'}^m(\tau_{d'j'} - \bar\tau_{b'i'})$$
$$\times \left(w_{ji}^{db} w_{j'i'}^{d'b'} - w_{j'i}^{d'b} w_{ji'}^{db'} \right) e^{-i\omega_m(\bar\tau_{bi} - \tau_{d'j'})}$$
$$\times \delta_{\alpha_1,\alpha_{dj}} \delta_{\bar\alpha_2,\bar\alpha_{bi}} \delta_{\alpha_3,\alpha_{d'j'}} \delta_{\bar\alpha_4,\bar\alpha_{b'i'}},$$

and

$$\left\langle G_{\alpha_1\bar\alpha_2}^l \right\rangle_c = -\frac{1}{\beta} \sum_b^{N_b} \sum_{ij}^{n_b} f_l^0(\tau_{bj} - \bar\tau_{bi}) w_{ji}^{bb} \delta_{\alpha_1,\alpha_{bj}} \delta_{\bar\alpha_2,\bar\alpha_{bi}}.$$

Here $w_{ji}^{db} = \delta_{b,d} M_{bj,bi}^{(n_b)}$, where the matrix $M^{(n_b)} = [F^{(n_b)}]^{-1}$ is the inverse of the hybridization function matrix $F^{(n_b)}$ for expansion order n_b. The imaginary times τ_{bi} and $\bar\tau_{bi}$ all vary in the interval $[0, \beta)$. The expression of $\left\langle \mathcal{C}_{\boldsymbol{\alpha}}^{l,l'}(\omega_m) \right\rangle_c$ given above accounts for symmetries in order to reduce the computation time. The letters b and d label the N_b blocks decoupled by symmetry; in the cases discussed here, e.g., the $\sigma = \uparrow$ and

$\sigma = \downarrow$ blocks are decoupled. Further optimization is obtained exploiting, when possible, symmetries in l, l', in order to reduce the number of coefficients to compute and/or the error bars. For the Hamiltonians considered in this paper, time-reversal and pair-exchange symmetries yield

$$\chi_{\alpha_1 \bar{\alpha}_2 \alpha_3 \bar{\alpha}_4}^{l,l'}(\omega_m) = \chi_{\alpha_4 \bar{\alpha}_3 \alpha_2 \bar{\alpha}_1}^{l',l}(\omega_m),$$

$$\chi_{\alpha_1 \bar{\alpha}_2 \alpha_3 \bar{\alpha}_4}^{l,l'}(\omega_m) = \left[\chi_{\alpha_3 \bar{\alpha}_4 \alpha_1 \bar{\alpha}_2}^{l',l}(\omega_m)\right]^*,$$

where we used $[\chi_{\alpha_1 \bar{\alpha}_2 \alpha_3 \bar{\alpha}_4}^{l,l'}(\omega_m)]^* = \chi_{\alpha_4 \bar{\alpha}_3 \alpha_2 \bar{\alpha}_1}^{l',l}(-\omega_m)$.

Once we obtained the local susceptibility tensor, in order to calculate $\chi_{\boldsymbol{\alpha}}(\mathbf{q}; \omega_m)$, we solve the Bethe-Salpeter equation in the local vertex approximation. Here the first step consists of rewriting the bubble term $\chi_{\boldsymbol{\alpha}}^{0;n,n'}(\mathbf{q}; \omega_m)$, where ν_n and ν'_n are fermionic Matsubara frequencies, in the chosen basis of functions. We do this via the transformation

$$\chi_{\boldsymbol{\alpha}}^{0;l,l'}(\mathbf{q}; \omega_m) = (-1)^{l'+m+1} \sum_{nn'} \left[T_{nl}^m\right]^* \chi_{\boldsymbol{\alpha}}^{0;n,n'}(\mathbf{q}; \omega_m) T_{n'l'}^m,$$

where

$$T_{nl}^m = \frac{1}{\beta} \int_0^\beta d\tau \, e^{i\nu_n \tau} f_l^m(\tau)$$

and

$$\chi_{\boldsymbol{\alpha}}^{0;n,n'}(\mathbf{q}; \omega_m) = -\beta \delta_{n,n'} \delta_{\sigma_1 \sigma_4} \delta_{\sigma_2 \sigma_3}$$

$$\times \frac{1}{N_{\mathbf{k}}} \sum_{\mathbf{k}} G_{\alpha_1 \bar{\alpha}_4}(\mathbf{k}; \nu_n) G_{\alpha_3 \bar{\alpha}_2}(\mathbf{k+q}; \nu_n + \omega_m).$$

Next, to obtain the **q**-dependent susceptibility we solve the set of matrix equations

$$[\chi(\mathbf{q}; \omega_m)^{-1}]_{N,N'} = [\chi^0(\mathbf{q}; \omega_m)^{-1}]_{N,N'} + [\Gamma(\omega_m)]_{N,N'},$$

$$[\Gamma(\omega_m)]_{N,N'} = [\chi(\omega_m)^{-1}]_{N,N'} - [\chi^0(\omega_m)^{-1}]_{N,N'},$$

$$[\chi^0(\omega_m)]_{N,N'} = \frac{1}{N_{\mathbf{q}}} \sum_{\mathbf{q}} [\chi^0(\mathbf{q}; \omega_m)]_{N,N'},$$

with $N = \alpha_1 l, \bar{\alpha}_2 l$ and $N' = \alpha_3 l', \bar{\alpha}_4 l'$. In the last step, the components of the physical two-particle Green's function tensor are obtained as follows:

$$\chi_{\boldsymbol{\alpha}}(\mathbf{q}; \omega_m) = \frac{1}{\beta^2} \sum_{ll'} f_l^{-m}(0^+) \chi_{\boldsymbol{\alpha}}^{l,l'}(\mathbf{q}; \omega_m) f_{l'}^{-m}(0^+), \quad \text{(B2)}$$

using the orthogonality properties of the polynomials. The convergence with increasing maximum polynomial order included in the sum, $l_{\max}$, is shown in Fig. 8. The coefficients $\chi_{\boldsymbol{\alpha}}^{l,l'}(\mathbf{q}; \omega_m)$ entering in this sum typically decay quickly with l, l', much faster than the corresponding coefficients in the Matsubara representation, $\chi_{\boldsymbol{\alpha}}^{n,n'}(\mathbf{q}; \omega_m)$. This speeds up the calculations considerably. In addition, to increase accuracy, we calculate via Eq. (B2) the difference $\chi_{\boldsymbol{\alpha}}^{l,l'}(\mathbf{q}; \omega_m) - \chi_{\boldsymbol{\alpha}}^{0;l,l'}(\mathbf{q}; \omega_m)$, which decays even faster, and add only at the end the value $\chi_{\boldsymbol{\alpha}}^0(\mathbf{q}; \omega_m)$ calculated with very high precision via Matsubara sums. The static susceptibilities calculated in this paper are obtained by setting $\omega_m = 0$ in the general formulas given in this Appendix.

[1] K. I. Kugel and D. I. Khomskii, Zh. Eksp. Teor. Fiz. **64**, 1429 (1973) [Sov. Phys. JETP **37**, 725 (1973)].

[2] D. I. Khomskii and K. I. Kugel, Solid State Commun. **13**, 763 (1973).

[3] J. Kanamori, J. Appl. Phys. **31**, S14 (1960); B. Halpering and R. Englman, Phys. Rev. B **3**, 1698 (1970).

[4] E. Pavarini, E. Koch, and A. I. Lichtenstein, Phys. Rev. Lett. **101**, 266405 (2008).

[5] E. Pavarini and E. Koch, Phys. Rev. Lett. **104**, 086402 (2010).

[6] E. Pavarini, S. Biermann, A. Poteryaev, A. I. Lichtenstein, A. Georges, and O. K. Andersen, Phys. Rev. Lett. **92**, 176403 (2004).

[7] H. Sims, E. Pavarini, and E. Koch, Phys. Rev. B **96**, 054107 (2017).

[8] K. Knox, J. Chem. Phys. **30**, 991 (1959).

[9] Y. Ito and J. Akimitsu, J. Phys. Soc. Jpn. **40**, 1333 (1976).

[10] K. Kaneko, G. Kuwabara, and A. Misu, Solid State Commun. **18**, 1085 (1976).

[11] P. J. Walker, J. Cryst. Growth **46**, 709 (1979).

[12] M. Hidaka and P. J. Walker, Solid State Commun. **31**, 383 (1979).

[13] M. Hidaka, K. Inoue, I. Yamada, and P. J. Walker, Phys. B (Amsterdam) **121**, 343 (1983).

[14] M. Totani, Y. Fukada, and I. Yamada, Phys. Rev. B **40**, 10577 (1989).

[15] H. Manaka, I. Yamada, T. Kitazawa, M. Kobayashi, M. Ishizuka, and S. Endo, J. Phys. Soc. Jpn. **66**, 2989 (1997).

[16] V. Ya. Mitrofanov, A. E. Nikiforov, and S. Yu. Shashkin, Solid State Commun. **104**, 499 (1997).

[17] M. Ishizuka, M. Terai, M. Hidaka, S. Endo, I. Yamada, and O. Shimomura, Phys. Rev. B **57**, 64 (1998).

[18] M. Ishizuka, M. Terai, S. Endo, M. Hidaka, I. Yamada, and O. Shimomura, J. Magn. Magn. Mater. **177–181**, 725 (1998).

[19] C. T. Liang and K. D. Schotte, J. Phys. Soc. Jpn. **74**, 3221 (2005).

[20] I. Yamada, J. Phys. Soc. Jpn. **33**, 979 (1972).

[21] M. Ishizuka, I. Yamada, K. Amaya, and S. Endo, J. Phys. Soc. Jpn. **65**, 1927 (1996).

[22] H. Manaka, Y. Miyashita, Y. Watanabe, and T. Masuda, J. Phys. Soc. Jpn. **76**, 044710 (2007).

[23] E. Herdtweck and D. Babel, Z. Anorg. Allg. Chem. **474**, 113 (1981).

[24] A. Flesch, E. Gorelov, E. Koch, and E. Pavarini, Phys. Rev. B **87**, 195141 (2013).

[25] C. Autieri, E. Koch, and E. Pavarini, Phys. Rev. B **89**, 155109 (2014).

[26] A. Flesch, G. Zhang, E. Koch, and E. Pavarini, Phys. Rev. B **85**, 035124 (2012).

[27] V. I. Anisimov, A. I. Poteryaev, M. A. Korotin, A. O. Anokhin, and G. Kotliar, J. Phys.: Condens. Matter **9**, 7359 (1997).

[28] A. I. Lichtenstein and M. I. Katsnelson, Phys. Rev. B **57**, 6884 (1998).

[29] E. Pavarini, E. Koch, D. Vollhardt, and A. Lichtenstein, editors, *The LDA+DMFT Approach to Strongly Correlated Materials* (Verlag des Forschungszentrum, Jülich, 2011).

[30] E. Pavarini, E. Koch, D. Vollhardt, and A. Lichtenstein, editors, *DMFT at 25: Infinite Dimensions* (Verlag des Forschungszentrum, Jülich, 2014).

[31] E. Pavarini, E. Koch, A. Lichtenstein, and D. Vollhardt, editors, *DMFT: From Infinite Dimensions to Real Materials* (Verlag des Forschungszentrum, Jülich, 2017).

[32] P. Blaha, K. Schwarz, G. K. H. Madsen, D. Kvasnicka, and J. Luitz, *WIEN2k, An Augmented Plane Wave + Local Orbitals Program for Calculating Crystal Properties* (Technische Universität Wien, Austria, 2001); P. Blaha, K. Schwarz, P. Sorantin, and S. Trickey, Comput. Phys. Commun. **59**, 399 (1990).

[33] N. Marzari and D. Vanderbilt, Phys. Rev. B **56**, 12847 (1997).

[34] For the Wannier90 code see A. A. Mostofi, J. R. Yates, Y.-S. Lee, I. Souza, D. Vanderbilt, and N. Marzari, Comput. Phys. Commun. **178**, 685 (2008).

[35] E. Gull, A. J. Millis, A. I. Lichtenstein, A. N. Rubtsov, M. Troyer, and P. Werner, Rev. Mod. Phys. **83**, 349 (2011).

[36] See, e.g., Chap. 6 in Ref. [30] for a pedagogical introduction.

[37] L. Boehnke, H. Hafermann, M. Ferrero, F. Lechermann, and O. Parcollet, Phys. Rev. B **84**, 075145 (2011).

[38] H. Shinaoka, J. Otsuki, M. Ohzeki, and K. Yoshimi, Phys. Rev. B **96**, 035147 (2017).

[39] A. Kiani and E. Pavarini, Phys. Rev. B **94**, 075112 (2016).

[40] D. I. Khomskii, *Transition Metal Compounds* (Cambridge University Press, 2014).

[41] For the derivation of the superexchange Hamiltonian for an idealized perovskite with $J \neq 0$, see Refs. [1, 2] and Ref. [42].

[42] A. M. Olés, L. F. Feiner, and J. Zaanen, Phys. Rev. B **61**, 6257 (2000).